# Damage detection and quantification via multiview DIC at varying scales

Israe Hamadouche, Darius Seyedi, François Hild

## To cite this version:

Israe Hamadouche, Darius Seyedi, François Hild. Damage detection and quantification via multiview DIC at varying scales. Experimental Mechanics, 2024, 64, pp.675-689. 10.1007/s11340-024-01038-0 . hal-04436627

# Damage detection and quantification via multiview DIC at varying scales

Israe Hamadouche[1,2], Darius M. Seyedi[1*] and François Hild[2]

[1*]Université Paris-Saclay, CEA, Service d'Etudes Mécanique et Thermique, Gif-sur-Yvette, 91191, France.
[2]Université Paris-Saclay, CentraleSupélec, ENS Paris-Saclay, CNRS LMPS-Laboratoire de Mécanique Paris-Saclay, 91191 Gif-sur-Yvette, France.

*Corresponding author(s). E-mail(s): darius.seyedi@cea.fr;

## Abstract

**Background:** To minimize measurement uncertainties and create seamless procedures between tests and simulations for the characterization and prediction of damage in large scale structures, a system capable of monitoring the quantities of interest at different scales throughout the test is required. **Objective:** The aim of this work is to develop a multiview DIC framework at varying scales in which kinematic fields are expressed on a unique mesh. **Methods:** A three-point flexural test was performed on a concrete beam and the images acquired by three different cameras were used to perform DIC calculations. **Results:** Displacement and strain fields were measured using mono and multiview implementations; their associated uncertainties were assessed. Damage initiation and growth within the sample was quantified based on the standard displacement uncertainty. **Conclusion:** The reported results show that the proposed method reduced the associated displacement uncertainties. The onset and propagation of damage was successfully quantified.

**Keywords:** Uncertainty quantification - Displacement - Calibration - Backtracking - Damage

# 1 Introduction

Reinforced-concrete (RC) structures represent a significant proportion of both conventional and industrial buildings. One of the main issues within these structures is their mechanical integrity, specifically to know whether the structure can continue to fulfill its function in extreme situations (such as earthquakes). Concrete is widely used in its nonlinear domain as RC structures are usually designed to allow cracking to occur under in-service loading [20]. Concrete exhibits a complex mechanical behavior with different sources of nonlinearity, namely, nonlinear and nonsymmetric stress-strain responses, tensile cracking and compressive crushing [5]. Nonlinear calculations are particularly useful in the seismic re-evaluation of a building as recommended in re-evaluation guides (e.g., FEMA 273 [1] and 356 [2], ATC 40 [4]). Such analyses allow for a better understanding of the behavior of structures by simulating the succession of phenomena characterizing the failure of each structural element.

Accurate modeling of damage in reinforced concrete structures under seismic loading remains a scientific and technical challenge especially for high damage levels. The complex response of RC structures to cyclic loadings often poses challenges in numerical analyses leading to instability. Achieving convergence becomes notably arduous when factors such as extensive cracking, rebar yielding, and rebar failure occur during such analyses [22]. Thus, experimental tests on large-scale specimens provide valuable information for a deeper understanding of the structural behavior and for validating numerical models. Detailed numerical simulations are performed to compare experimental and numerical results for validating constitutive models [25]. A good understanding of the material behavior and structural response during such tests calls for measurements at different scales [23].

In experimental solid mechanics, optical measurement methods are utilized for deformation quantification and allow for non-contact extraction of full-field information [11]. One of the most commonly used techniques is Digital Image Correlation (DIC) [29, 28]. In the civil engineering field, among other vision-based techniques [16], DIC has often been used for displacement and strain measurements. It has been employed for the study of brittle and quasi-brittle materials. For instance, Wu et al. [33] investigated the properties of fracture process zones (FPZs) in concrete. DIC was used to determine the FPZ length and crack opening displacements. In the work of Li et al. [19], DIC allowed crack initiation and propagation to be evaluated in nano-particles modified recycled aggregate concrete (RAC) in order to experimentally study their effects on the microstructual properties of RAC. To understand the mechanical performance of an ultra-high performance engineered cementitious composite (UHP-ECC), Yu et al. [35] used DIC to simultaneously monitor multiple crack patterns. In other papers, DIC has been combined with acoustic emission (AE) techniques to monitor damage processes in concrete and mortar. For concrete, the combination of DIC and AE proved to be effective in identifying fracture parameters and cracking mechanisms by measuring crack openings at different locations [3]. In the work of Rouchier et al. [26], DIC enabled for the monitoring of progressive damage development in fiber reinforced mortar. Displacement maps revealed various ranges of cracks from microscopic to macroscopic scales. Similar studies could be carried out under dynamic loading conditions as it was the case in the paper of Xing et al. [34]. Stereocorrelation was used to capture strain and strain rate fields of a rock. The DIC method was compared to stain gauge data. The results revealed that the strain gauge signals were unable to accurately measure the actual strain on the brittle material.

All the papers cited above used monoview DIC. Very little work has been reported on the use of DIC at different scales. Yet, the use of several cameras with different resolutions and covering large parts of tested structures is desirable. The development of a multiview [8] framework at varying scales is the aim of the present work. Multiscale and multiview DIC approaches were developed separately in previous works. Measurement uncertainties in DIC depend on the number of pixel per the size of subsets in the local approaches [32, 31, 17] or element size in global approaches [15, 6]. For a given resolution, bigger elements contain more pixels and thus yield lower measurement uncertainties. However, capturing sharp displacement gradients or discontinuities in measured fields calls for fine meshes, (i.e., lower number of pixels per element), which increase the measurement uncertainties. To overcome this limitation, Passieux et al. [23] developed a nearfield/farfield multiscale DIC approach. Two cameras with two different resolutions were used. At the farfield, a series of images captured the whole specimen surface. Another series of images acquired by a second camera with a higher resolution zoomed on a smaller part of the specimen. The nearfield/farfield analyses were treated independently. A multiscale transformation was determined to register the nearfield and farfield reference images. It was deduced that the multiscale approach lowered the measurement uncertainties. An interesting follow-up is to be able to take advantage of the redundancy in areas that are monitored by more than one camera. It can be achieved by coupling multiview approaches at varying scales in a unique framework.

Developing such framework is the main topic of the paper whose outline is as follows. First, a short overview of digital image correlation is given and more specifically monoview and FE-based DIC. The second section is dedicated to multiview DIC, where the different steps are detailed. Next, the experimental setup is presented and the approach is applied to a three-point flexural test performed on a concrete beam. Mono-view DIC calculations are run on different sets of images acquired with three cameras. The measurement uncertainties are evaluated on a sequence of images of the unloaded beam. Then, the displacement fields assessed from monoview DIC and with the multiview approach are compared. Because strain fields are very useful to study crack initiation and propagation [3, 19, 26, 33, 34, 35], they are used to quantify damage in the reported experiment.

## 2 Monoview digital image correlation

Monoview digital image correlation consists in measuring the displacement field $\boldsymbol{u}$ by correlating one image $I_0$ of the reference configuration with another $I_t$ in the deformed configuration. The underlying principle of DIC is the gray level conservation that should be satisfied at each pixel position $\boldsymbol{x}$

$$I_0(\boldsymbol{x}) = I_t[\boldsymbol{x} + \boldsymbol{u}(\boldsymbol{x})] \tag{1}$$

To determine the unknown displacement field $\boldsymbol{u}$, the sum of squared differences $\phi_c^2$ is minimized

$$\phi_c^2 = \frac{1}{2\sigma_c^2} \int_{ROI} (I_t[\boldsymbol{x} + \boldsymbol{u}(\boldsymbol{x})] - I_0(\boldsymbol{x}))^2 d\boldsymbol{x} \tag{2}$$

where ROI stands for the whole region of interest, and $\sigma_c$ the standard deviation of acquisition noise (of camera $c$) that is assumed to be white and Gaussian. The displacement field is parameterized as

$$\boldsymbol{u}(\boldsymbol{x}) = \sum_p \upsilon_p \boldsymbol{\psi}_p(\boldsymbol{x}) \tag{3}$$

where $\upsilon_p$ are the unknown nodal degrees of freedom, and $\boldsymbol{\psi}_p$ the corresponding shape functions. The unknowns that are determined in the minimization scheme are all degrees of freedom gathered in the column vector $\{\boldsymbol{\upsilon}\}$.

The correlation residual $\rho$

$$\rho(\boldsymbol{x}) = I_0(\boldsymbol{x}) - I_t[\boldsymbol{x} + \boldsymbol{u}(\boldsymbol{x})] \tag{4}$$

is computed for each pixel position $\boldsymbol{x}$. This quality estimator detects any local mismatch between the experimental and assumed kinematics. For instance, the presence of a crack induces a displacement discontinuity that is generally not included a priori in the sought displacement field. Hence, damage can be tracked with such field that is computed at the pixel scale in addition to element-wise fields such as the maximum principal strains [12].

A DIC setting is an inverse problem, which is ill-posed in Hadamard's sense. As a consequence, the FE discretization cannot be made as fine as possible since the measurement uncertainties would drastically increase [13]. It is worth noting that FE-based DIC already includes a (hard) regularization since the measured displacement field is a priori continuous over the considered ROI. An additional ingredient is to add mechanical regularization [24], which filters out displacement fluctuations that are not mechanically admissible. A penalty term is thus added to the DIC cost function $\phi_c^2$, which is based on the equilibrium gap [7]

$$\phi_m^2 = \{\boldsymbol{\upsilon}\}^\top [\boldsymbol{K}]^\top [\boldsymbol{K}] \{\boldsymbol{\upsilon}\} \tag{5}$$

where $[\boldsymbol{K}]$ is the stiffness matrix. This penalization is applied to inner nodes and force-free boundaries. For Dirichlet boundary nodes, another regularization is necessary, where a penalization of short wavelength traction fluctuations is performed

$$\phi_b^2 = \{\boldsymbol{\upsilon}\}^\top [\boldsymbol{K}]^\top [\boldsymbol{L}] [\boldsymbol{K}] \{\boldsymbol{\upsilon}\} \tag{6}$$

where $[\boldsymbol{L}]$ is the Laplace-Beltrami operator [21].

The total cost function $\phi_t^2$ is introduced when the correlation residuals $\phi_c^2$, equilibrium gap $\phi_m^2$ and boundary fluctuations $\phi_b^2$ are minimized simultaneously

$$(1 + \omega_m + \omega_b)\phi_t^2 = \widetilde{\phi_c^2} + \omega_m \widetilde{\phi_m^2} + \omega_b \widetilde{\phi_b^2} \tag{7}$$

with $\widetilde{\phi}_c$, $\widetilde{\phi}_m$ and $\widetilde{\phi}_b$ defined as

$$\widetilde{\phi}_c = \frac{\{\boldsymbol{v}\}[\boldsymbol{H}]\{\boldsymbol{v}\}}{\{\boldsymbol{w}\}[\boldsymbol{H}]\{\boldsymbol{w}\}} \ , \ \widetilde{\phi}_m = \frac{\phi_m(\{\boldsymbol{v}\})}{\phi_m(\{\boldsymbol{w}\})} \ , \ \widetilde{\phi}_b = \frac{\phi_b(\{\boldsymbol{v}\})}{\phi_b(\{\boldsymbol{w}\})} \tag{8}$$

where $\boldsymbol{w}$ is a trial displacement field defined for normalization purposes in the form of a pure shear wave [30]

$$\boldsymbol{v}(\boldsymbol{x}) = \sin(2\pi \boldsymbol{k}\boldsymbol{x}) \tag{9}$$

The weights $\omega_m$ and $\omega_b$ are defined as functions of the characteristic lengths $\ell_m$ and $\ell_b$ respectively, called regularization lengths

$$\omega_m = (2\pi|\boldsymbol{k}|\ell_m)^4 \tag{10}$$

and

$$\omega_b = (2\pi|\boldsymbol{k}|\ell_b)^4 \tag{11}$$

where $\boldsymbol{k}$ is the wave vector. The higher the regularization lengths $\ell_m$ and $\ell_b$, the more weight is put on the corresponding cost functions.

## 3 Multiview framework

As opposed to a regular DIC with a single camera, the present multiview system requires additional steps to be able to express the results in a unique frame, which is covering the entire surface of the sample. The starting point consists in meshing the numerical model. Before performing multiview DIC (M-DIC), a calibration step is necessary. Since multiple cameras are used to capture different zones of the sample surface, each set of pictures is expressed in its own frame (in pixels). This frame being different from the physical one (in metric units), a first step consists in defining which zones of the mesh are seen by each camera and calibrating the system via DIC. Transformation functions must be identified to relate images acquired by each camera to the master mesh. These transformation functions must account for scaling factors, rotation angles and translations related to each camera so as the meshes can be positioned on the reference images. The following step, called backtracking, helps to properly overlay the images and their corresponding meshes. The scaling factors are also updated at the end of this step. Next, in order to prepare for M-DIC, the acquisition noise related to each camera is estimated and the computation of the Hessian matrices for each camera and the global Hessian matrix $[\boldsymbol{H}]$ are required. Then, M-DIC proceeds by computing the right-hand side vectors related to each camera and for each iteration, and then assembling the global right-hand side vector $\{\boldsymbol{h}\}$. Last, the displacement increments of each image state are updated. A flowchart displaying the algorithm of M-DIC is shown in Figure 1.

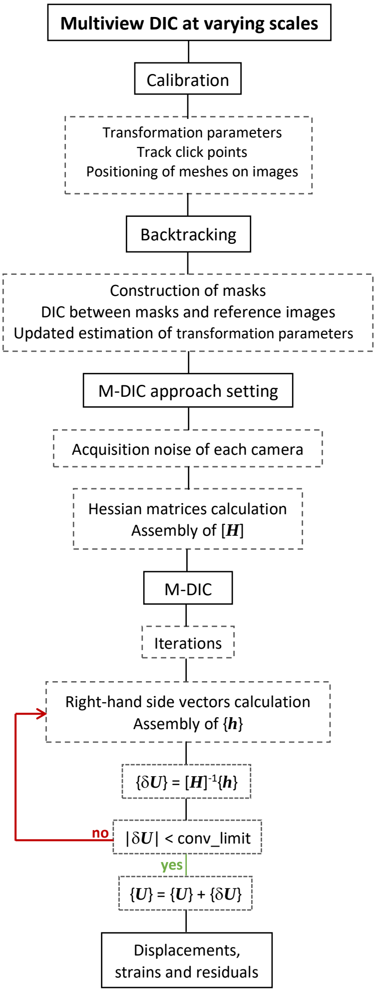

**Fig. 1** Flowchart of the multiview DIC algorithm.

## 3.1 Calibration procedure

In general, two calibration routes are followed depending on the considered test case. The conventional procedure is called self-calibration [9]. The latter may be chosen if there is an adequacy between the mesh and the real geometry. In that case, the self-calibration points are easily identifiable in the ROI. However, in the case when the geometric shape of the structure is a bit more complex, a so-called hybrid calibration is carried out. A calibration target with known dimensions is used and moved in the experimental environment such that all the cameras capture the entire geometry of the target.

At the end of this step, a first estimation of transformation matrix related to each camera is deduced. The transformation is applied to the meshes related to each camera in order to switch from node coordinates expressed in the physical frame (i.e., in mm) to those in the image frame (in pixels). To be able to properly position the meshes on the images, a backtracking procedure was necessary to fine tune the previously determined transformation parameters.

## 3.2 Backtracking procedure

From the previous information, the following step, called backtracking, is performed. It consists in running a DIC analysis between the image of the initial configuration of any camera and its corresponding mask based on the numerical mesh. The mask is constructed from the physical mesh by considering only the pixels that belong to the sample surface. Then the mask is deformed so that it fits the actual shape of the sample. The transformation between the image (acquired by camera $c$) and physical frames is defined as

$$\begin{Bmatrix} x^c \\ y^c \end{Bmatrix} = [\boldsymbol{F}^c] \begin{Bmatrix} X - X_0^c \\ Y - Y_0^c \end{Bmatrix} \tag{12}$$

where $\boldsymbol{F}^c$ defines a homography

$$\boldsymbol{F^c} = S^c \boldsymbol{R}(\theta^c) \tag{13}$$

$x^c$ and $y^c$ are the nodal coordinates of the mesh in the image frame, $X$ and $Y$ their corresponding positions in the physical (i.e. metric) space (in mm), $X_0^c, Y_0^c$ the translations in the x and y-directions, $S^c$ the scaling factor (expressed in px/mm for each camera $c$), and $[\boldsymbol{R}(\theta^c)]$ the rotation matrix

$$[\boldsymbol{R}(\theta^c)] = \begin{bmatrix} \cos\theta^c & \sin\theta^c \\ -\sin\theta^c & \cos\theta^c \end{bmatrix} \tag{14}$$

with $\theta^c$ the rotation angle.

A specific procedure was applied to get initial estimates of the transformation parameters (i.e. scaling factors and rotation angles). Once this step is completed, the mesh is laid over the reference picture of each camera. Updated and more precise values of the set of scaling factors are obtained at the end of the backtracking step.

## 3.3 Multiview approach

In a multiview framework, the minimization of the weighted cost functions for each camera (defined in Equation (2)) has to take into account the transformation matrices $[\boldsymbol{F}^c]$. Hence, the global M-DIC cost function reads

$$\phi_M^2(\{\boldsymbol{U}\}) = \sum_{c=1}^{n} \frac{1}{2\sigma_c^2} \int_{ROI^c} \left(I_0^c(\boldsymbol{x}^c(\boldsymbol{X})) - I_t^c(\boldsymbol{x}^{\boldsymbol{c}}(\boldsymbol{X}) + \boldsymbol{F}^c\boldsymbol{U}(\boldsymbol{X}, \{\boldsymbol{U}\}))\right)^2 d\boldsymbol{X} \tag{15}$$

where the column vector $\{\boldsymbol{U}\}$ gathers all unknown degrees of freedom (expressed in mm) of the sought displacement field $\boldsymbol{U}$, $I_t^c$ the gray levels associated with the image of the deformed configuration with respect to the reference ones $I_0^c$ of camera $c$.

From the cost function (15), the Hessian matrices need to be computed for each camera. Since they are based on the reference configurations [14], they are only computed once and for all. Because each camera is different, all images are affected by acquisition noise that is specific to each of them. The Hessian matrices, when constructed from the cost function (15), are simply summed since $\sigma_c$ is already included. The second member vector needs to be updated since the gray level residuals $\rho_c$ are computed after each iteration. As soon as the norm of the displacement increment is less than the convergence limit, the iteration loop stops and the measured displacement field $\boldsymbol{U}$, expressed in mm, is deduced.

# 4 Experimental application

To validate the M-DIC approach, a three-point flexural test was performed on a notched concrete beam with dimensions $835 \times 105 \times 100$ mm (Figure 2(a)). The notch was 5 mm wide and 25 mm deep. The speckle pattern can be applied in various ways. On the one hand, the size of the speckles must be fine enough to adapt the spatial resolution of the measurement to the studied phenomenon. On the other hand, it must be large enough to be correctly resolved with respect to acquisition noise. In the present experimental test, a regular pattern was first provided with a grid on which the black paint was sprayed. Some randomization then was introduced to the pattern, by adding some random stripes (Figure 2(b)). The speckle pattern in the central region where the notch was located was more refined because it was the most likely to experience crack initiation and propagation. Therefore, a more refined analysis of this area was required. Figure 2(c) displays the different areas of the sample surface that were monitored by the three cameras. The areas close to the outer span were observed by a single camera, while the central part was visible by the three cameras.

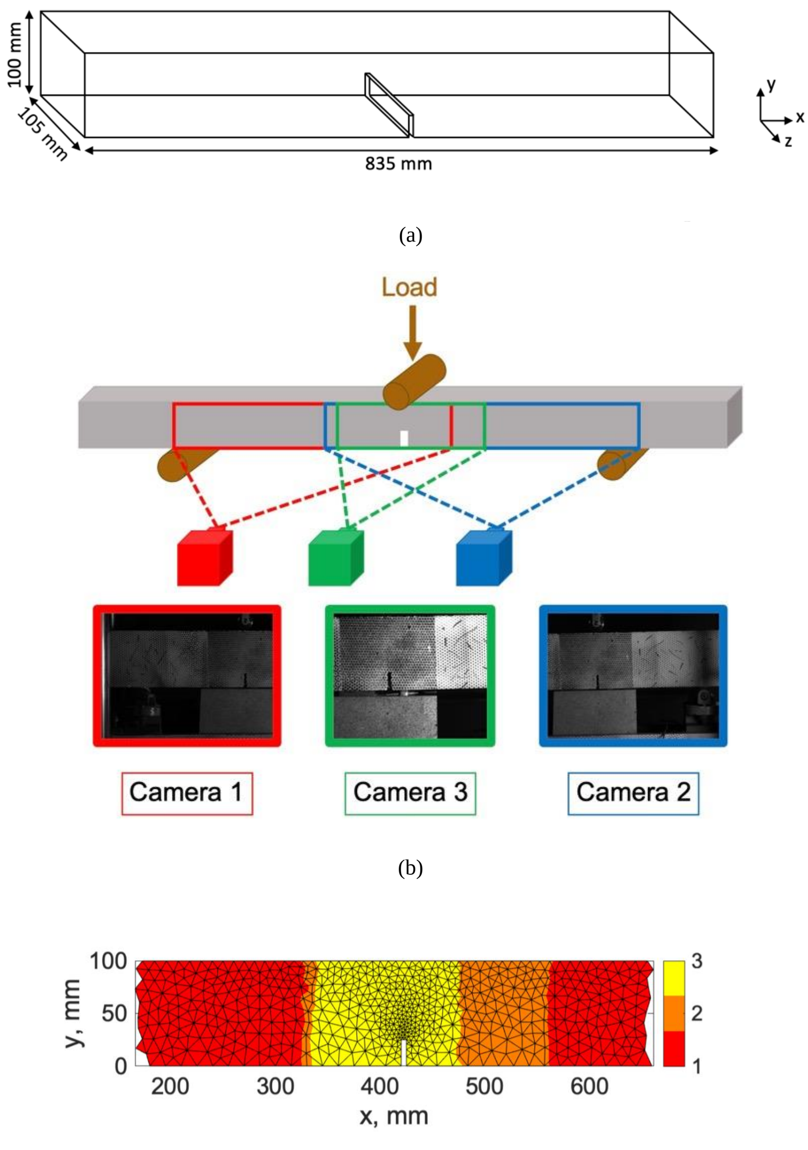

(a)

(b)

(c)

**Fig. 2** (a) Dimensions of the studied notched concrete beam. (b) Schematic view of the 3-point flexural test monitored by three different cameras. (c) Number of cameras that capture each area of the surface of the sample.

## 4.1 Experimental setup

Three 8-bit digitization cameras were placed at different locations, with no tilt, to monitor different zones of the sample surface (Figure 2(b,c)). All three cameras captured a common region of interest, which is the notched zone. Reflections on the right side of the sample were caused by the lighting source positioned toward this side. Table 1 gathers the hardware parameters of present setup.

**Table 1** DIC hardware parameters of the multiview system

| | Camera 1 | Camera 2 | Camera 3 |
|---|---|---|---|
| Camera type | Canon EOS 70D | Canon EOS 90D | Manta |
| Definition | 2748 × 1835 pixels | 3492 × 2330 pixels | 1390 × 1038 pixels |
| Color filter | none | none | none |
| Gray Levels rendering | 8 bits | 8 bits | 8 bits |
| Lens | Canon EF 24 mm | Canon EF 24 mm | Canon EF 50 mm |
| Aperture | f/2.8 | f/2.8 | f/1.8 |
| Field of view | 275 mm × 184 mm = 0.05 m$^2$ | 349 mm × 233 mm = 0.08 m$^2$ | 139 mm × 104 mm = 0.01 m$^2$ |
| Image scale | 0.12 mm/px | 0.10 mm/px | 0.16 mm/px |
| Stand-off distance | between 80 and 100 cm | between 80 and 100 cm | between 80 and 100 cm |
| Image acquisition rate | 1/7 fps | 1/7 fps | 1 fps |
| Patterning technique | B/W paints | B/W paints | B/W paints |
| Mean pattern feature radius | 15 pixels | 11 pixels | 8 pixels |

An acquisition rate of one image each 7 s was chosen for the two Canon cameras (cameras 1 and 2) due to transfer limitations. A faster acquisition rate (1 fps) was selected for the Manta camera (3). The fact that each camera was different in terms of definition and thus resolution made the experimental setup multiview and at varying scales. In multiview DIC, the synchronization of the cameras is critical and any time lag between the cameras will result in errors in DIC measurements. The sample was subjected to a flexural loading controlled by the notch opening displacement measured with an LVDT sensor. The maximum force reached 3700 N.

Each camera acquired a sequence of images of the surface of interest (cameras 1 and 2 captured a total of 138 pictures, while camera 3 acquired 863). For measurement uncertainty quantification, sequences of images of the reference configuration were acquired by the three cameras beforehand.

## 4.2 Monoview DIC results

The Correli 3.0 framework, which is developed at LMPS, was used [18]. This library provides a platform within which to build DIC codes in Matlab. Table 2 gathers the monoview DIC parameters for the three cameras.

**Table 2** Monoview DIC analysis parameters for cameras 1, 2 and 3 respectively

| | |
|---|---|
| DIC software | Correli 3.0 [18] |
| Image filtering | None |
| Element sizes | $\approx$ 53 px / $\approx$ 63 px / $\approx$ 39 px |
| Shape functions | Linear (T3 elements) |
| Matching criterion | Sum of squared differences (2) |
| Interpolant | Spline |
| Displacement noise-floor | 0.07 px / 0.04 px / 0.03 px |

As a first analysis, the FE mesh of the geometry was projected onto the reference images of each camera and DIC calculations were run on each set of images independently. The global (physical) mesh was created with Gmsh [10]. The mean element size was chosen to be equal to 6 mm, namely, not to be too large to get resolved displacement and strain fields but not too small not to cover the speckle pattern. Since the images were acquired by three different cameras, the physical pixel sizes were not identical. Additionally, the different sets of images were not affected by the same acquisition noise.

In the following, only direct calculations are reported in which each considered picture was registered with respect to the reference image. In Figure 3, the red, blue and green zones are related to cameras 1, 2 and 3, respectively. The three horizontal displacement maps show very high displacement gradients, which reveal the presence of a crack in the notch area along the height of the sample. A small rotation is noticed in the fields with respect to the horizontal axis especially for cameras 2 and 3. This effect will be taken into account in the following section where M-DIC is described.

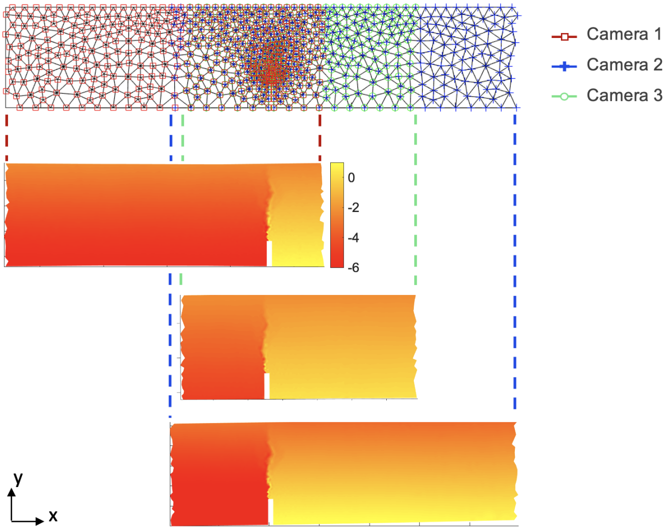

**Fig. 3** Horizontal displacement fields (expressed in pixels) resulting from monoview DIC analyses associated with each camera.

## 4.3 Multiview DIC

In the present case, since the tested geometry was suitable, a self-calibration procedure was performed. The transformation between the mesh of the numerical model (whose nodal coordinates are expressed in mm) and the image (in pixels) is described in equations (12), (13) and (14).

This process takes into account the translations in both $x$ and $y$-directions, the scaling factor and the rotation about $z$. Since each camera captured the entire height of the sample and the notch, one way to estimate the scale factor was to measure the height of the sample on each image via Perspective-n-Point (PnP) analyses. Then, since the physical distance is known, a simple conversion between pixel and physical lengths is obtained and the scale factors related to all three cameras are deduced. One has to note that these values are just first order estimations and need to be updated afterward (Table 3).

**Table 3** Estimations of transformation parameters for the three cameras

| | Camera 1 | Camera 2 | Camera 3 |
|---|---|---|---|
| Initial scaling factor (px/mm) | 8.29 | 10.33 | 6.08 |
| Updated scaling factor (px/mm) | 8.28 | 10.31 | 6.08 |
| Rotation angle (rad) | $-0.001$ | 0.016 | 0.013 |

To be able to properly position the meshes on the images, a few points of interest that can be easily tracked on both configurations are considered. Since the notched area of the sample was captured by all three cameras and because the notch physical dimensions are known, two points at the bottom of the notch are selected on the mesh and also on the reference pictures of each camera (Figure 4).

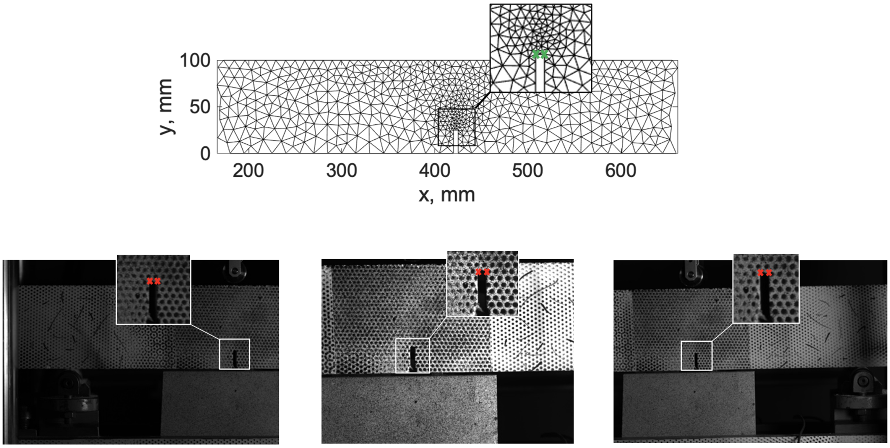

**Fig. 4** Selected points on the FE mesh (green) and on reference pictures of each camera (red).

Since the notch dimensions are quite small compared to the entire structure dimensions, the points are very close. Therefore, the positioning of the mesh on each image is not perfect and some small rotations are observed (Figure 5). Thus, the proposed backtracking procedure was implemented.

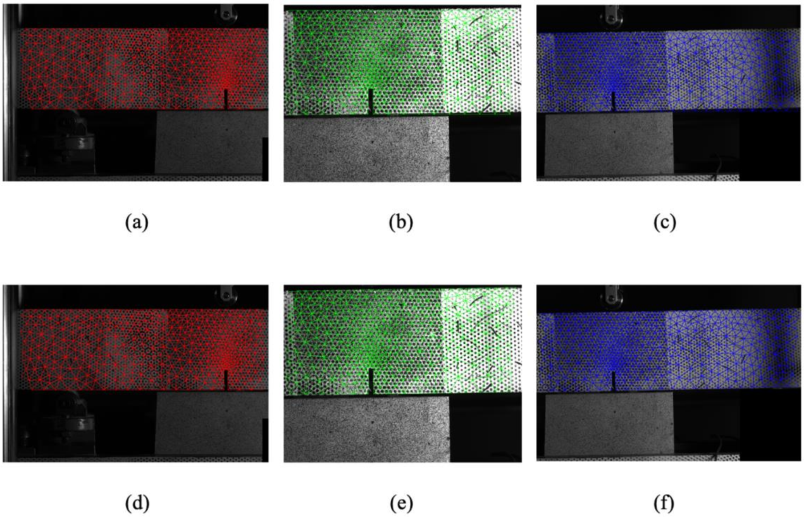

**Fig. 5** First row: approximate positioning of the mesh on the reference image of cameras 1 (a), 3 (b) and 2 (c). Second row: Overlay of final backtracked meshes and reference images of cameras 1 (d), 3 (e) and 2 (f).

To run the backtracking procedure, a very coarse (auxiliary) mesh was created. This auxiliary mesh was used to register the mask with respect to the reference image of each camera. The resulting displacements were used to deform the coarse mesh, which is now in the physical frame. For any point belonging to the auxiliary mesh, it is thus possible to find its position in the image frame (by applying the opposite displacement). Thus, all the nodes of the nominal mesh are backtracked toward the image frame. By repeating this procedure for each camera, the master mesh was backtracked and adjusted on the initial configurations (Figure 5).

At the end of backtracking, the overlay of the three meshes on the images has improved. However, the rotation angles associated with each camera are yet to be found. To do so, a Gauss-Newton scheme was used to determine the desired parameters, namely, the scaling factors and rotation angles from the deformed mesh with respect to the reference mesh. This scheme being iterative, the initial values of the scaling factors were those found at the end of the PnP procedure. The rotation angles were initialized by approximately estimating the tilt of the beam with respect to the horizontal axis within the reference images captured by each camera.

The final values are obtained once the convergence criterion was reached (i.e., $10^{-6}$ rad). Last, the mesh is adjusted by applying the corrected transformation parameters (i.e., scaling factors and rotation angles). Table 4 displays the DIC analysis parameters that were used for the multiview approach.

**Table 4** M-DIC analysis parameters

| | |
|---|---|
| DIC software | Correli 3.0 [18] |
| Image filtering | None |
| Mean element size | ≈ 6.3 mm (see Figure 4) |
| Shape functions | Linear (T3 elements) |
| Matching criterion | Sum of squared differences (15) |
| Interpolant | Linear |
| Displacement noise-floor | 4 µm |

## 4.4 Uncertainty quantification

A set of 50 images of the reference configuration were acquired by the three cameras before loading the specimen for uncertainty quantification purposes. In order to estimate the acquisition noise that affected each camera, a mono-view DIC analysis was run. Ideally, the displacements should be the smallest possible. However, one lighting device was placed near camera 2, which led to an over-exposure in that area resulting in some relatively "high" displacements in comparison with the rest of the surface.

Figure 6 displays the histograms of gray level residuals for each camera. These residuals are rather small, yet not zero, which indicates that the images associated with the three cameras were affected by acquisition noise. Their mean values are close to zero. Their standard deviations are 1.1, 0.9 and 2 gray levels for cameras 1, 2 and 3, respectively.

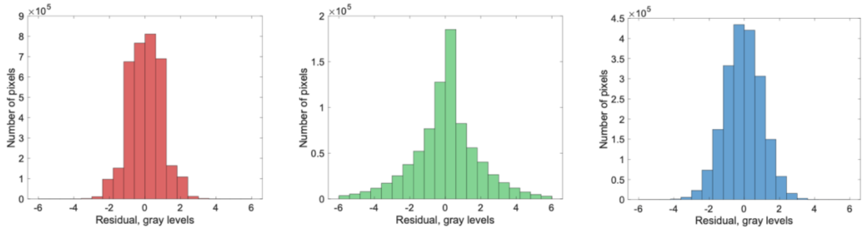

(a) (b) (c)

**Fig. 6** Gray level residual histograms associated with acquisition noise of cameras 1 (a), 3 (b) and 2 (c)

To compare monoview and multiview results, a unique displacement output (m-DIC) is computed. In m-DIC, the nodal displacements are first measured for each camera independently. The m-DIC estimate is then obtained as the weighted average with respect to the number of cameras (Figure 2(c)). To estimate the measurement uncertainties associated with m-DIC and M-DIC, the standard horizontal and vertical displacement uncertainties that resulted from both DIC approaches are shown in Figure 7. All the fields presented herein are displayed in the unique global mesh whose coordinates are expressed in the physical frame (i.e., in mm). In both cases, some of the displacement fluctuations are due to the controller of the hydraulic system as the testing machine was on. Yet, these values remain very small (i.e., less than 8 µm).

The differences between both fields, which are shown in Figure 7, reveal a clear difference in the central area. In the monovision areas, the difference is vanishing since m-DIC and M-DIC are strictly equivalent when only one camera is involved. Additionally, the area that was captured by two cameras displayed some scattered differences of about 0.5 µm in both horizontal and vertical directions. Furthermore, the central area where the system is multiview (i.e., 3 cameras), the highest difference is observed, namely, 2.5 µm for the horizontal component and 0.7 µm for the vertical one.

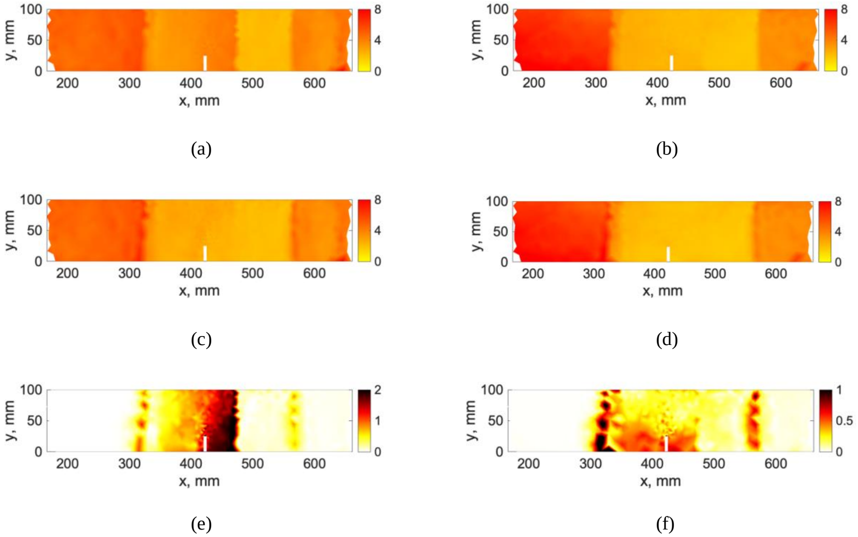

(a) (b) (c) (d) (e) (f)

**Fig. 7** Standard displacement uncertainty fields (expressed in µm) associated with m-DIC (first row), M-DIC (second row), and corresponding differences (third row). (a,c,e) Horizontal and (b,d,f) vertical displacement components.

The maps displayed in Figure 7(e,f) highlight the fact that the use of several cameras and the developed M-DIC framework leads to a decrease in measurement uncertainties in the areas monitored by several cameras. The zone where three cameras are involved shows better results than those with two cameras. In fact, the more cameras monitor a given zone, the lower the measurement uncertainties. This result stems from the fact that the global Hessian matrix is the sum of the (semi-positive definite) Hessian matrices of each individual camera, and the covariance matrix of the measured degrees of freedom is proportional to the inverse of the Hessian matrix [6]. Therefore, M-DIC helps to improve the trustworthiness of the measured displacements by decreasing their uncertainties.

## 4.5 Monoview and M-DIC displacement measurements

In the present experiment, one key quantity of interest is the notch opening displacement (NOD). It is retrieved from the measured displacements in the vicinity of the notch. As shown in Figure 8(a), two areas, 15 mm in length and height, are selected on the left and right sides of the notch. The horizontal displacements of the nodes belonging to these areas are used for the NOD calculations. Their mean values are computed over each area and the NOD then is the difference between these two values. Figure 8(b) shows a virtually constant rate of the NOD throughout the test, which is consistent with the way the test was controlled. At the end of the test, when the crack has traversed the whole sample height, the NOD is no longer increasing with time. All reported results will be shown with respect to the NOD history.

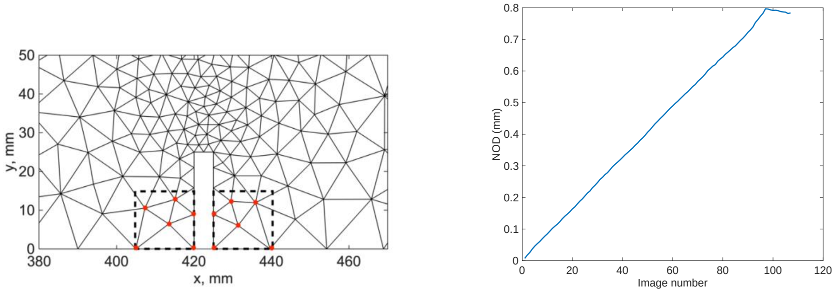

(a) (b)

**Fig. 8** (a) Nodes considered to evaluate the Notch Opening Displacement (NOD). (b) NOD (expressed in mm) as a function of image number.

The quality of the registration is evaluated by assessing the gray level residual fields, which correspond to the difference, in gray levels, between the reference picture and the deformed image corrected by the measured displacement. In Figure 9, the dimensionless RMS residual level is plotted for the sequence of 107 images as a function of the Notch Opening Displacement (NOD) for m-DIC and M-DIC. To get dimensionless values, the RMS gray level residuals are normalized with respect to the RMS residuals of M-DIC performed on the 50 images of the reference configuration. Fine and coarse meshes are considered. The element size of the coarse mesh is equal to 6 mm, while the finer one had an element size of 2.5 mm. The coarse mesh was initially used to develop the M-DIC approach. All curves have the same trend, which starts with a small normalized RMS level of about 2.1 for m-DIC and 1.6 for M-DIC. It then sharply increases in the first few steps (until the NOD reaches about 50 µm). This trend is due to crack initiation and fast propagation (see Figure 14(b)). Then, the slope becomes less steep yet still increases slowly. Some fluctuations are noticed for the last few steps, which reflects the end of crack propagation.

Figure 9 shows that the m-DIC measurements lead to higher residual levels compared to M-DIC. This is to be expected since M-DIC aims for minimizing these residuals, contrary to m-DIC that minimizes individually the gray level residuals, but not globally. Another observation is that improving the spatial resolution (by refining the mesh discretization) allowed the residual levels to be lowered.

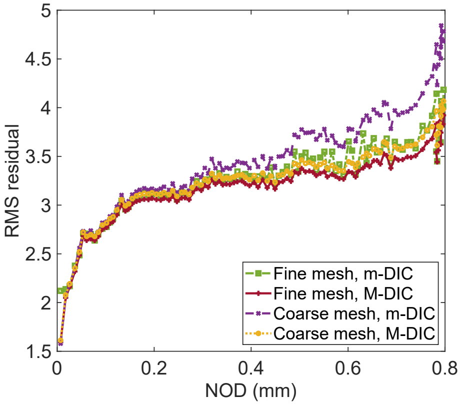

**Fig. 9** Dimensionless RMS residuals obtained for various DIC analyses performed on a set of 107 images. m-DIC and M-DIC stand for combined monoview and multiview DIC, respectively.

Figure 10(a,b) displays the displacement field that was measured via M-DIC. As was observed in the displacement maps of m-DIC (Figure 3), the horizontal displacement field reveals the presence of damage in the notched area. This damage corresponds to a crack that initiated and propagated from the notch root essentially along the vertical direction. The vertical displacement field is also similar to those measured for each camera separately and corresponds to a flexure kinematics.

For comparison purposes, Figure 10(c,d) shows the displacement fields obtained when performing DIC calculations on each camera independently and projecting the results in the global frame on the unique mesh. For the regions monitored by more than one camera, the nodal displacement was averaged according to the number of cameras.

When comparing the results obtained in both cases (Figure 10(a,b) and Figure 10(c,d)), no large differences occur. However, by computing to the displacement difference

$$\boldsymbol{u}_{dif} = \boldsymbol{u}_M - \boldsymbol{u}_m \tag{16}$$

it is noted that the main difference in the fields (Figure 10(e,f)) occur in the overlapping areas where two or three cameras are involved (Figure 2(c)). For both horizontal and vertical displacement fields, the main difference is present in the cracked region where the three cameras are involved. In particular, the crack path is noticeable on the horizontal displacement map. When comparing both results to the measurement uncertainties, one notes that the horizontal displacement difference is about 20 times the standard uncertainties while the vertical one is about 5 times the standard uncertainties. This result shows that the two approaches are not statistically equivalent, and that M-DIC performed better than averaged monoview DIC since the corresponding gray level residuals were lower for M-DIC (Figure 9).

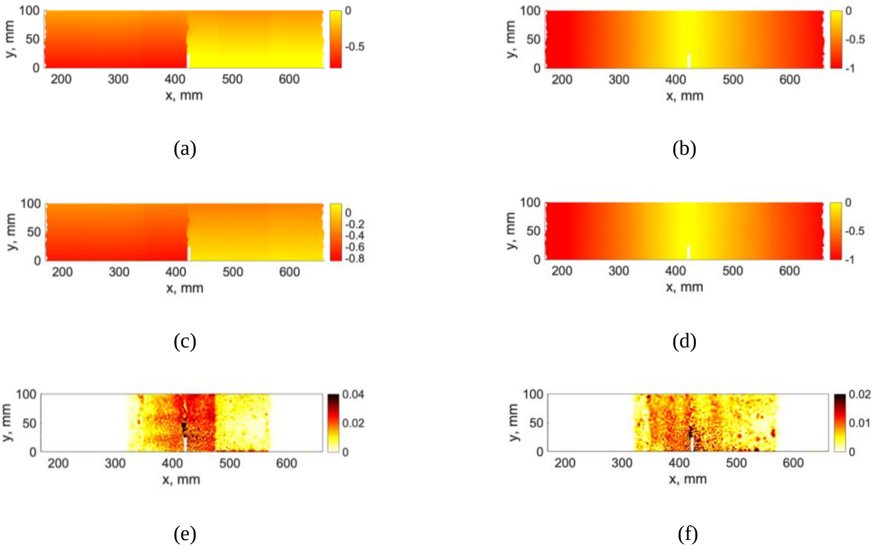

(a) (b)

(c) (d)

(e) (f)

**Fig. 10** Displacement fields (expressed in mm) at the end of the experiment measured via m-DIC (first row), averaged M-DIC (second row), and corresponding differences (third row). (a,c,e) Horizontal and (b,d,f) vertical displacement components.

## 4.6 Mechanical regularization and damage localization

To illustrate the effect of regularization, a large regularization length is considered in the DIC calculation, namely, 4 times the element size. Figure 11 shows this effect on the standard displacement uncertainties of M-DIC. When comparing these maps with unregularized results (Figure 7), it is observed that the discontinuities between zones observed by different cameras is mitigated thanks to mechanical regularization.

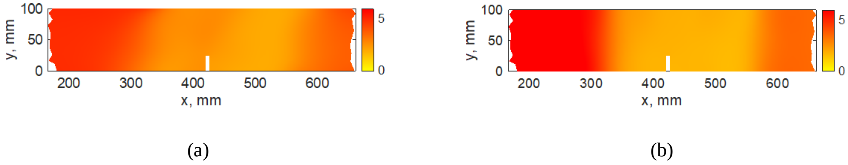

(a) (b)

**Fig. 11** Regularized standard displacement uncertainties of M-DIC (expressed in µm) (a) Field in the x-direction (b) field in the y-direction ($L_{reg}$ = 4 × the element size).

Another example of the effect of mechanical regularization is shown in Figure 12. The longitudinal strain field obtained with unregularized M-DIC and the associated regularized field are displayed. The elements with very high strain values are those considered as damaged. A crack appears in Figure 12(a), in addition to some rather high strain values in the transition area between the zone that was monitored with one camera and that with two cameras. Figure 12(b) on the other hand illustrates how mechanical regularization leads to smoother fields that filtered out high frequency fluctuations due to measurement uncertainties but also smeared the crack over the regularization length.

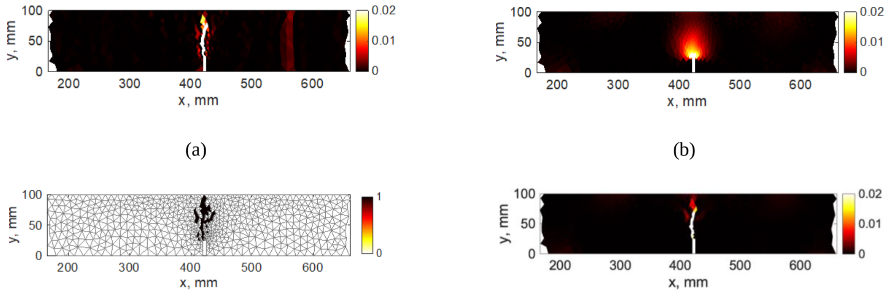

(a)

(b)

(c)

(d)

**Fig. 12** (a) Unregularized $\epsilon_{xx}$ strain field. (b) Regularized $\epsilon_{xx}$ strain field ($L_{reg} = 4\times$ element size). (c) Damaged elements for the last image of the test ($k = 22$). (d) Regularized strain field $\epsilon_{xx}$ ($L_{reg} = 4\times$ element size) with a damage criterion.

A particular approach has been implemented in the present case to perform selective regularization. An unregularized DIC analysis is first run and the elements where a crack is present are found by applying a detection criterion on the strain field. A threshold strain was set as a function of the standard strain uncertainty. The damage variable $D$ is set to 1 when the normal strain $\epsilon_{xx}$ is greater than $k = 22$ times its standard uncertainty. As explained in Section 2, mechanical regularization is used to filter out displacement fluctuations that are not mechanically admissible. This regularization is not applied on the damaged elements. The value of $k$ is chosen to decrease the non-physical fluctuations of the displacement field on the one hand, and to detect localized damage initiation and growth on the other hand.

Figure 12(c) displays the damaged elements where the crack is visible in addition to two small side cracks that initiated but did not propagate as much as the main one that took over. In the present case, the spurious fluctuations in the fields are filtered out everywhere but in the damaged elements where the regularization was fully discarded.

Figure 12(d) displays the horizontal strain field $\epsilon_{xx}$ deduced from a regularized M-DIC calculation coupled with the damage criterion (Figure 12(c)). The crack path appears very clearly and corresponds to the elements with the highest strain levels. Coupling regularized DIC with a damage criterion (Figure 12(c)) leads to a smoother and noise-mitigated strain field while still keeping the crack path very localized.

The dimensionless RMS residuals are displayed in Figure 13 when three DIC calculations are run. Regularized M-DIC leads to the highest residual levels. This result is due to mechanical regularization that acts as a low-pass filter (Figure 12(b)). The higher the regularization length, the stronger the filter and therefore the higher the residuals. Unregularized M-DIC and m-DIC yield lower values. More specifically, M-DIC has lower residual levels than m-DIC since the global residuals are the quantity that is minimized contrary to m-DIC that minimized the same quantity but for each camera independently. By introducing a damage criterion in regularized M-DIC, the RMS residuals are significantly reduced in comparison with regularized M-DIC. The fact that m-DIC and M-DIC with damage essentially coincide is not believed to be general. However, it shows that even though regularization was added, the use of damage lowered drastically the RMS residuals in comparison with the same case with no damage criterion.

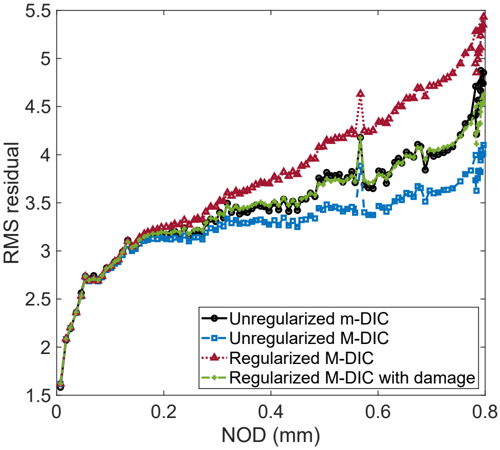

**Fig. 13** Dimensionless RMS residual obtained for m-DIC and M-DIC for three different cases of mechanical regularization.

M-DIC has the advantage of assessing the damage state of the whole studied ROI throughout the entire test. The damaged elements were labeled at each loading step and their corresponding surface was deduced. Figure 14(a) shows a gradual growth of the cumulative surface of the damaged elements. This quantity is made dimensionless by dividing it by the total surface of the beam. At the end of the test, the cumulative surface reached approximately 1.7% of the total surface of the beam. In the last part of the experiment, for NODs greater than 0.53 mm, it levels off. This trend is due to the fact that the crack fully propagated through the height of sample.

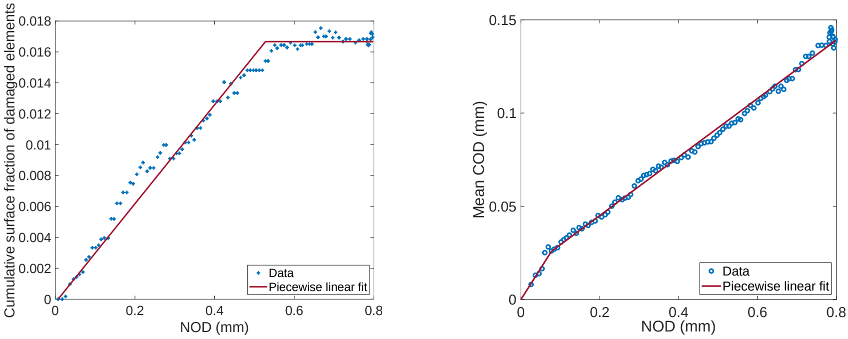

(a) (b)

**Fig. 14** (a) Cumulative dimensionless surface of damaged elements as a function of notch opening displacement (NOD) and its corresponding piecewise linear fit. (b) Mean crack opening displacement (COD) vs. notch opening displacement (NOD) and its corresponding piecewise linear fit.

Figure 14(b) presents the history of the mean crack opening displacement. The COD is defined as the normal strain $\epsilon_{xx}$ multiplied by the element size [27]. By interpolating the measured data with a piecewise linear function, two regimes are observed. The first one characterizes crack initiation (with a steep slope). Then, the second part (with a lower slope) corresponds to crack propagation.

# 5 Conclusion

A multiview DIC framework was applied at varying scales. To validate the new approach, a three-point flexural test was performed on a concrete beam. Three cameras with three different resolutions (i.e., by a factor 1.7 in the present case) were involved. A global FE mesh of the surface of the sample, whose coordinates were expressed in a unique physical frame, was used for the DIC calculations. M-DIC required a calibration step since multiple cameras monitored different zones of the sample surface. It enabled scale factors and rotation angles to be deduced. Mesh backtracking was performed to overlay the images and the corresponding visible portions of the master mesh.

Uncertainties were quantified by acquiring 50 pictures of the reference configuration and performing mono-scale M-DIC analyses. In areas monitored by more than one camera, the standard displacement uncertainties were higher for combined monoview DIC (m-DIC) compared to M-DIC. M-DIC allowed these uncertainties to be significantly reduced (by a factor 2).

Displacement fields were measured for the whole test and displayed for the final state. The RMS residuals were lower in M-DIC. A case study with two discretizations showed that the finer mesh led to lower residual levels as it could better capture the three cracks. Mechanical regularization was also introduced in M-DIC analyses. When coupled with a damage criterion, it led to better results. The regularized

Multiscale and Multiview DIC approach lead to the highest residual levels in comparison with other cases (unregularized monoview DIC and unregularized M-DIC). Coupling mechanical regularization with a damage criterion allowed these levels to be significantly reduced. Last, thanks to the developed M-DIC framework, a damage analysis was carried out. The damaged elements at each deformed state were retrieved and the cumulated damaged surface and the corresponding mean crack opening displacement could be assessed.

Although the experimental test is 3D by nature, the optical setup remained 2D since all the cameras were placed perpendicular to the surface of the beam. 3D multiscale and multiview correlation could also be performed by tilting the cameras to capture out-of-plane motions. The DIC framework introduced herein can be generalized to account for such situations. In addition, large-scale complex structures could then be monitored. The camera resolutions could be very different, varying from local to global scales. The different scales would allow for analyses to be extremely focused in damaged regions while enabling for the boundary conditions to be measured throughout the test.

## Acknowledgments

This work was supported by CEA (French Alternative Energies and Atomic Energy Commission) and Paris-Saclay SEISM Institute (https://www.institut-seism.fr/en/).

## Declaration

**Conflict of Interest:** The authors declare that they have no conflict of interest.

# References

[1] FEMA 273. Nehrp guidelines for seismic rehabilitation of buildings. Technical report, Federal Emergency Management Agency, 1997.

[2] FEMA 356. Prestandard and commentary for the seismic rehabilitation of buildings. Technical report, Federal Emergency Management Agency, 2000.

[3] S.Y. Alam, J. Saliba, and A. Loukili. Fracture examination in concrete through combined digital image correlation and acoustic emission techniques. Construction and Building Materials, pages 232–242, 2014.

[4] ATC-40. Seismic evaluation and retrofit of concrete buildings. Technical report, Applied Technology Conucil, 1996.

[5] K. Bathe, J. Walczak, A. Welch, and N. Mistry. Nonlinear analysis of concrete structures. Computers & Structures, pages 563–590, 1989.

[6] M. Berny, T. Archer, P. Beauchêne, A. Mavel, and F. Hild. Displacement uncertainty quantifications in t3-stereocorrelation. Experimental Mechanics, page 771–790, 2021.

[7] D. Claire, F. Hild, and S. Roux. A finite element formulation to identify damage fields: The equilibrium gap method. Int. J. Num. Meth. Engng., 61(2):189–208, 2004.

[8] J.-E. Dufour, F. Hild, and S. Roux. Shape, Displacement and Mechanical Properties from Isogeometric Multiview Stereocorrelation. Journal of Strain Analysis for Engineering Design, 50(7):470–487, 2015.

[9] O.D. Faugeras, Q.T. Luong, and S.J. Maybank. Camera self-calibration: Theory and experiments. In Proc. 2nd ECCV, pages 321–334. Springer-Verlag, 1992.

[10] C. Geuzaine and J.-F. Remacle. Gmsh: A 3-d finite element mesh generator with built-in pre- and post-processing facilities. International Journal for Numerical Methods in Engineering, pages 1309–1331, 2009.

[11] M. Grédiac and F. Hild, editors. Full-Field Measurements and Identification in Solid Mechanics. ISTE / Wiley, London (UK), 2012.

[12] F. Hild, A. Bouterf, and S. Roux. Damage Measurements via DIC. International Journal of Fracture, 191(1-2):77–105, 2015.

[13] F. Hild and S. Roux. Comparison of local and global approaches to digital image correlation. Experimental Mechanics, 52(9):1503–1519, 2012.

[14] F. Hild and S. Roux. Digital image correlation. In P. Rastogi and E. Hack, editors, Optical Methods for Solid Mechanics. A Full-Field Approach, pages 183–228, Weinheim (Germany), 2012. Wiley-VCH.

[15] F. Hild and S. Roux. Displacement uncertainties with multiview correlation schemes. Journal of Strain Analysis for Engineering Design, 55(7-8):199–211, 2020.

[16] B.F. Spencer Jr, V. Hoskere, and Y. Narazaki. Advances in computer vision-based civil infrastructure inspection and monitoring. Engineering, pages 199–222, 2019.

[17] X.-D. Ke, H. W. Schreier, M. A. Sutton, and Y. Q. Wang. Error Assessment in Stereo-based Deformation Measurements. Experimental Mechanics, 51(4):423–441, 2011.

[18] H. Leclerc, J. Neggers, F. Mathieu, F. Hild, and S. Roux. Correli 3.0. IDDN.FR.001.520008.000.S.P.2015.000.31500, Agence pour la Protection des Programmes, Paris (France), 2015.

[19] W. Li, C. Long, V.W.Y. Tam, C.-S Poon, and W. Hui Duan. Effects of nano-particles on failure process and microstructural properties of recycled aggregate concrete. Construction and Building Materials, pages 42–50, 2017.

[20] M. Matallah, C. La Borderie, and O. Maurel. A practical method to estimate crack openings in concrete structures. International Journal for Numerical and Analytical Methods in Geomechanics, pages 1615–1633, 2010.

[21] A. Mendoza, J. Schneider, E. Parra, and S. Roux. The correlation framework: Bridging the gap between modeling and analysis for 3D woven composites. Composite Structures, 229:111468, 2019.

[22] C. Mourlas, G. Markou, and M. Papadrakakis. Accurate and computationally efficient nonlinear static and dynamic analysis of reinforced concrete structures considering damage factors. Engineering Structures, pages 258–285, 2019.

[23] J.-C. Passieux, F. Bugarin, C. David, J.-N. Périé, and L. Robert. Multiscale displacement field measurement using digital image correlation: Application to the identification of elastic properties. Experimental Mechanics, pages 121–137, 2015.

[24] J. Réthoré, S. Roux, and F. Hild. An extended and integrated digital image correlation technique applied to the analysis fractured samples. European Journal of Computational Mechanics, 18:285–306, 2009.

[25] B. Richard, S. Cherubini, F. Voldoire, P.-E. Charbonnel, T. Chaudat, S. Abouri, and N. Bonfils. Smart 2013: Experimental and numerical assessment of the dynamic behavior by shaking table tests of an asymmetrical reinforced concrete structure subjected to high intensity ground motions. Engineering Structures, pages 99–116, 2016.

[26] S. Rouchier, G. Foray, N. Godin, M. Woloszyn, and J.-J Roux. Damage monitoring in fibre reinforced mortar by combined digital image correlation and acoustic emission. Construction and Building Materials, pages 371–380, 2013.

[27] V.F. Sciuti, F. Hild, V.C. Pandolfelli, T. Santos, B. Smaniotto, and R.B. Canto. Digital Image Correlation applied to in situ evaluation of surface cracks upon curing of MgO-containing refractory castables. Journal of the European Ceramic Society, 41(1):1003–1014, 2021.

[28] M.A. Sutton. Computer vision-based, noncontacting deformation measurements in mechanics: A generational transformation. Applied Mechanics Reviews, 65(AMR-13-1009):050802, 2013.

[29] M.A. Sutton, J.J. Orteu, and H. Schreier. Image correlation for shape, motion and deformation measurements: Basic Concepts, Theory and Applications. Springer, New York, NY (USA), 2009.

[30] Z. Tomičević, F. Hild, and S. Roux. Mechanics-aided digital image correlation. Journal of Strain Analysis for Engineering Design, 48:330–343, 2013.

[31] Y.-Q. Wang, M. A. Sutton, X.-D. Ke, H. W. Schreier, P. L. Reu, and T. J. Miller. On Error Assessment in Stereo-based Deformation Measurements. Experimental Mechanics, 51(4):405–422, 2011.

[32] Y.Q. Wang, M.A. Sutton, H.A. Bruck, and H.W. Schreier. Quantitative error assessment in pattern matching: Effects of intensity pattern noise, interpolation, strain and image contrast on motion measurements. Strain, 45:160–178, 2009.

[33] Z. Wu, H. Rong, J. Zheng, F. Xu, and W. Dong. An experimental inverstigation on the fpz properties in concrete using digital image correlation technique. Engineering Fracture Mechanics, pages 2978–2990, 2011.

[34] H.Z. Xing, Q.B Zhang, D. Ruan, S. Dehkhoda, G.X. Lu, and J. Zhao. Full-field measurement and fracture characterisations of rocks under dynamic loads using high-speed three-dimensional digital image correlation. International Journal of Impact Engineering, pages 61–72, 2018.

[35] K.-Q. Yu, J.-T Yu, J.-G. Dai, Z.-D. Lu, and S.P. Shah. Development of ultra-high performance engineered cementitious composites using polyethylene (pe) fibers. Construction and Building Materials, pages 217–227, 2018.